# $^{26}$Mg nuclear structure from $^{26}$Mg(200 MeV)+$^{208}$Pb scattering

D. C. Hensley, E. E. Gross, M. L. Halbert, J. R. Beene, and F. E. Bertrand
*Oak Ridge National Laboratory, Oak Ridge, Tennessee 37831*

G. Vourvopoulos and D. L. Humphrey
*Western Kentucky University, Bowling Green, Kentucky 42101*
(Received 3 December 1990)

Differential cross sections are reported for elastic scattering and for exciting the $2_1^+$ (1.81 MeV), $2_2^+$ (2.94 MeV), $4_1^+$ (4.32 MeV), and the $4_2^+$ (4.90 MeV) states of $^{26}$Mg from $^{26}$Mg (200 MeV)+$^{208}$Pb scattering. In addition, we have measured complete particle-$\gamma$ angular correlations for the $2_1^+ \rightarrow 0_1^+$, $2_2^+ \rightarrow 2_1^+$, and $4_2^+ \rightarrow 2_1^+$ $\gamma$ decays. Coupled-channels analysis was performed to extract $E2$ and $E4$ matrix elements. For the ground-state rotational band we find $M(E2;0_1^+ \leftrightarrow 2_1^+) = -16.79 \pm 0.13$ $e$ fm$^2$, $M(E4;0_1^+ \leftrightarrow 4_2^+) = +95 \pm 10$ $e$ fm$^4$, and $Q_2(2_1^+) = -20.9 \pm 1.9$ $e$ fm$^2$, where we have identified the $4_2^+$ (4.90 MeV) state as a member of the ground-state band rather than the $4_1^+$ (4.32 MeV) state. The $2_2^+$ (2.94 MeV) state is not well accounted for by the asymmetric-rotor model.

## I. INTRODUCTION

In a prior publication,[1] we presented a new technique for performing inelastic-scattering experiments and applied the method to the low-lying states of $^{24}$Mg excited in $^{24}$Mg(200 MeV)+$^{208}$Pb scattering. The technique consists in using a $4\pi$ $\gamma$-ray detector, the Spin Spectrometer (SS), to detect the decay $\gamma$ rays in coincidence with scattered projectiles detected in position-sensitive silicon-surface-barrier detectors. The $\gamma$-ray detectors provide the necessary resolution to resolve the excited states while the silicon detectors provide the information for the differential cross section. The technique also provides particle-$\gamma$ angular-correlation information which proves to be sensitive to the static quadrupole moment of the first $2^+$ state.[2] Here we apply the technique to the low-lying states of $^{26}$Mg. After presenting experimental details and the data, we report an extensive coupled channels analysis of the elastic scattering, and the differential cross sections for exciting the $2_1^+$(1.81 MeV), $2_2^+$(2.94 MeV), $4_1^+$(4.32 MeV), and the $4_2^+$(4.90 MeV) states (see level scheme in Fig. 1), as well as the particle-$\gamma$ angular correlations for the decay of the $2_1^+$, $2_2^+$, and $4_2^+$ states. The $^{26}$Mg level scheme, Fig. 1, has been difficult to understand from the nuclear-structure point of view particularly as to the nature of the second $2^+$ state (i.e., whether or not this state can be ascribed to a triaxial shape configuration for $^{26}$Mg) and as to which, if any, of the two low-lying $4^+$ states belong to the ground-state rotational band. The present data and analysis contribute towards resolving both questions. Finally, we compare nuclear-structure information extracted from these data and analysis with other reported measurements and with theory.

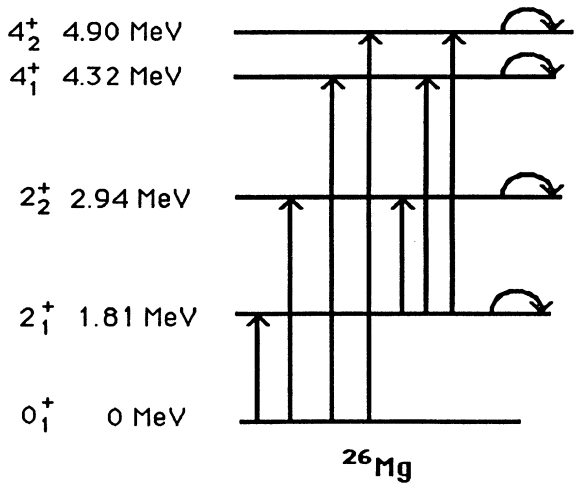


FIG. 1. $^{26}$Mg levels and transitions explicitly accounted for in the present coupled-channels analysis. All multipole orders up to $l=8$ were included in the symmetric-rotor-model calculations.

## II. DATA

A beam of 200.05 MeV $^{26}$Mg was provided by the HHIRF tandem accelerator. The target consisted of 400 $\mu$g/cm$^2$ of $^{208}$Pb evaporated on the downstream side of a 20-$\mu$g/cm$^2$ carbon foil. The mean beam energy at the center of the $^{208}$Pb target was 199.6±0.2 MeV. The inelastically scattered $^{26}$Mg ions were detected in position-sensitive solid-state detectors (PSD) in two different experimental arrangements. In one arrangement, a PSD was mounted in a 1.6-m-diam chamber and used to measure the angular distribution of elastically and inelastically scattered $^{26}$Mg ions. In the other arrangement, two PSD's, covering the entire angular range of interest in the 33-cm-diam scattering chamber of the SS, detected scattered $^{26}$Mg ions in coincidence with $\gamma$ rays in the SS. The $\gamma$-ray measurement provided, with good efficiency, the necessary energy resolution to resolve

 

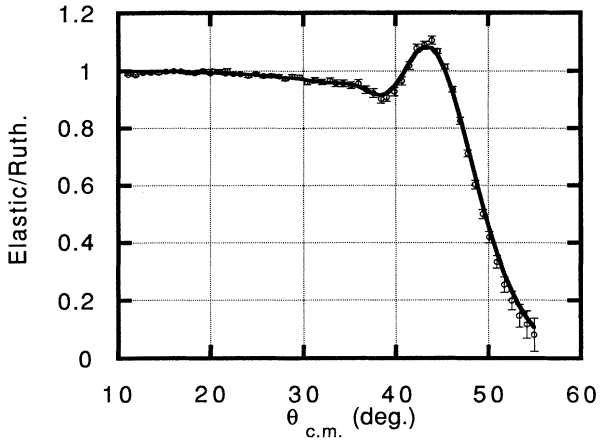


FIG. 2. Measured $^{26}$Mg(200 MeV)+$^{208}$Pb elastic scattering relative to Rutherford scattering (open circles). The solid curve represents the best coupled-channels fit to all the differential cross-section and particle-$\gamma$ angular-correlation data using symmetric-rotor-model form factors for all the matrix elements shown in Fig. 1.

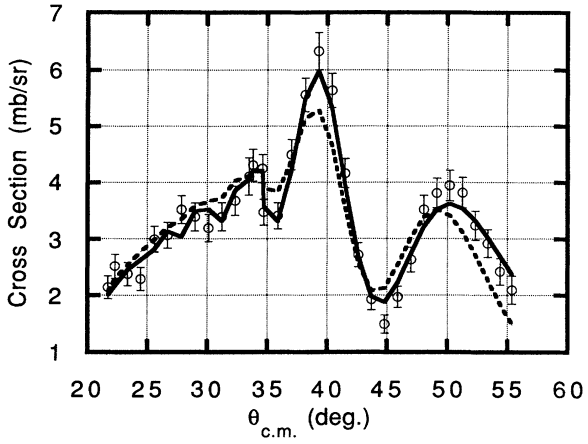


FIG. 4. Measured differential cross section (open circles) for exciting the $^{26}$Mg $2_2^+$(2.94 MeV) state by 200 MeV $^{26}$Mg scattering from $^{208}$Pb. The solid curve represents the best coupled-channels fit to all the differential cross-section and particle-$\gamma$ angular-correlation data using symmetric-rotor-model form factors for all the matrix elements shown in Fig. 1. The dashed curve represents the minimum-$\chi^2$ fit by varying the parameter $\gamma(=6°)$ of the asymmetric-rotor model.

the low-lying states of $^{26}$Mg. Most importantly, the elastic scattering at small angles, in the Coulomb-dominated region, served to provide an accurate absolute normalization. The details of how the two measurements were used to obtain the differential cross sections were described previously.[1]

The $^{26}$Mg levels observed with sufficient yield to determine the cross section were the ground state (elastic scattering), and the $2_1^+$(1.81 MeV), $2_2^+$(2.94 MeV), $4_1^+$(4.32 MeV), and $4_2^+$(4.90 MeV) excited states. Elastic scattering, displayed as a ratio to Rutherford scattering, is shown in Fig. 2 and the differential cross sections for the excited states are shown in Figs. 3–6. The discrete nature of the SS, 70 individual NaI detectors in a spherical array, allowed the particle-$\gamma$ angular correlation, $W(\theta_\gamma,\phi_\gamma)$, to be constructed for the $2_1^+$, $2_2^+$, and $4_2^+$ states. Choosing a laboratory system where $\theta_\gamma$ and $\phi_\gamma$ are the polar and azimuthal angles of the decay $\gamma$ ray with respect to the recoil $^{26}$Mg direction, we can express the correlation function as[3]

$$W(\theta_\gamma,\phi_\gamma)=\sum_{\substack{k=0,2,4,\ldots \\ -k\le q\le k}}\left[\frac{4\pi}{2k+1}\right]^{1/2} t_{kq}R_k\,Y_{kq}(\theta_\gamma,\phi_\gamma)\ , \tag{1}$$

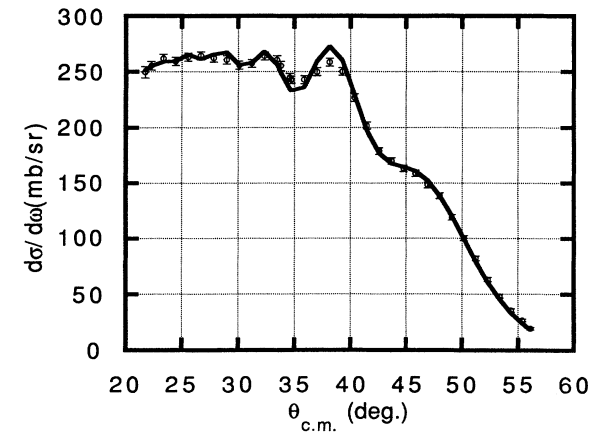


FIG. 3. Measured differential cross section, open circles, for exciting the $^{26}$Mg $2_1^+$(1.81 MeV) state by 200 MeV $^{26}$Mg scattering from $^{208}$Pb. The solid curve represents the best coupled-channels fit to all the differential cross-section and particle-$\gamma$ angular-correlation data using symmetric-rotor-model form factors for all the matrix elements shown in Fig. 1.

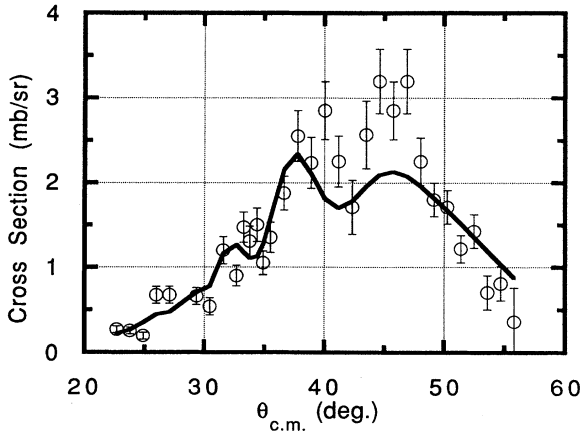


FIG. 5. Measured differential cross section (open circles) for exciting the $^{26}$Mg $4_1^+$(4.32 MeV) state by 200 MeV $^{26}$Mg scattering from $^{208}$Pb. The solid curve represents the best coupled-channels fit to all the differential cross-section and particle-$\gamma$ angular-correlation data using symmetric-rotor-model form factors for all the matrix elements shown in Fig. 1.

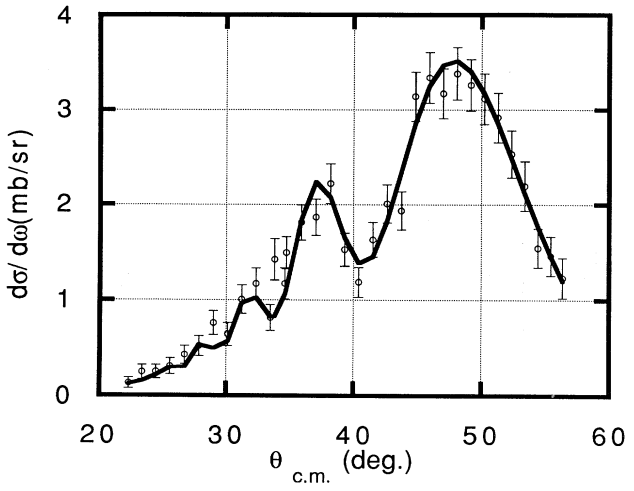


FIG. 6. Measured differential cross section (open circles) for exciting the $^{26}$Mg $4_2^+$(4.90 MeV) state by 200 MeV $^{26}$Mg scattering from $^{208}$Pb. The solid curve represents the best coupled-channels fit to all the differential cross-section and particle-$\gamma$ angular-correlation data using symmetric-rotor-model form factors for all the matrix elements shown in Fig. 1.

where the $R_k$ are tabulated $\gamma$-ray correlation coefficients[4] and the $t_{kq}(\theta_\gamma,\phi_\gamma)$ are alignment tensors, defined in Ref. 3, that describe the nuclear alignment prior to the decay of the state. In fitting this expression to the observed $\gamma$-ray angular correlation to obtain $(t_{kq})_{\rm exp}$, we take into account the attenuation due to the finite solid angle of each detector. The resulting alignment tensors are shown in Fig. 7 for the $2_1^+ \rightarrow 0_1^+$ decay $\gamma$, in Fig. 8 for the $2_2^+ \rightarrow 2_1^+$ decay $\gamma$, and in Fig. 9 for the $4_2^+ \rightarrow 2_1^+$ decay $\gamma$.

## III. ANALYSIS

### A. Elastic scattering

The differential cross-section data were analyzed in a rotational-model coupled-channels calculation for all the matrix elements indicated in Fig. 1 using the program ECIS.[5] As discussed in Sec. III C below, a few vibrational-model calculations were performed in an attempt to better describe the $2_2^+$ state alignment tensors. Many lengthy calculations were involved, searching over various combinations of the optical model parameters and matrix elements, but with so many parameters, the entire $\chi^2$ space was not investigated. Rather the search-

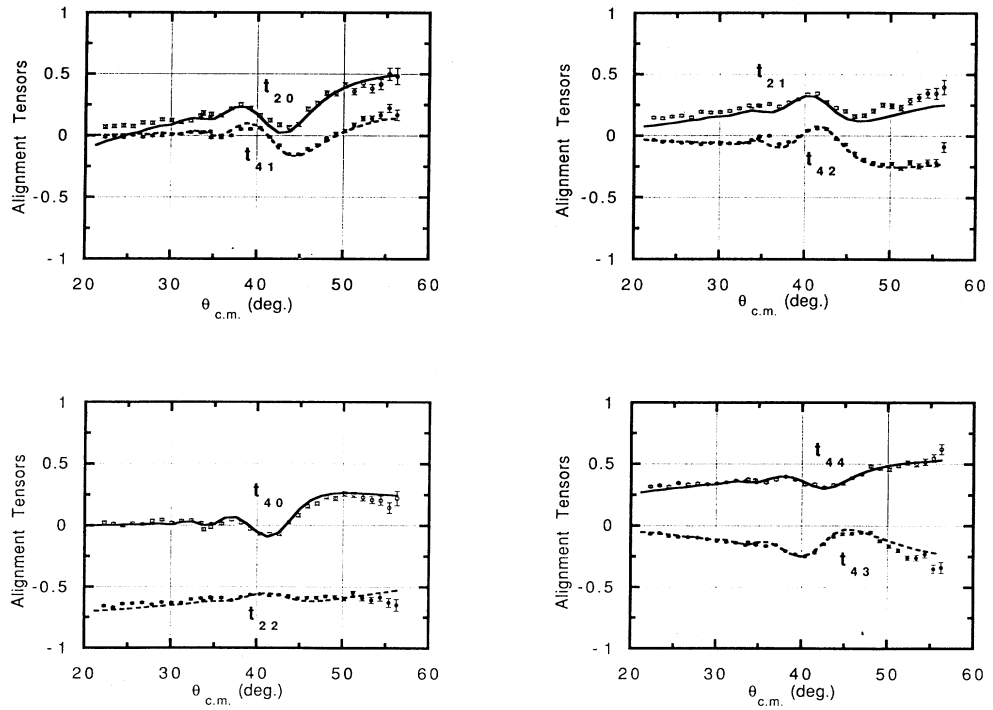


FIG. 7. Alignment tensors $t_{kq}$ for the decay of the $2_1^+$(1.81 MeV) state of $^{26}$Mg excited by 200 MeV $^{26}$Mg+$^{208}$Pb scattering as a function of c.m. scattering angle. The data, open and closed circles, come from fitting Eq. (1) to the measured particle-$\gamma$ angular-correlation data. The curves in each panel represent the best coupled-channels fit to all the differential cross-section and particle-$\gamma$ angular-correlation data using symmetric-rotor-model form factors for all the matrix elements shown in Fig. 1. Hyperfine attenuation of the original alignment was accounted for by normalizing the calculation to the data in the Coulomb-dominated region, $\theta_{\rm c.m.} \leq 35°$.

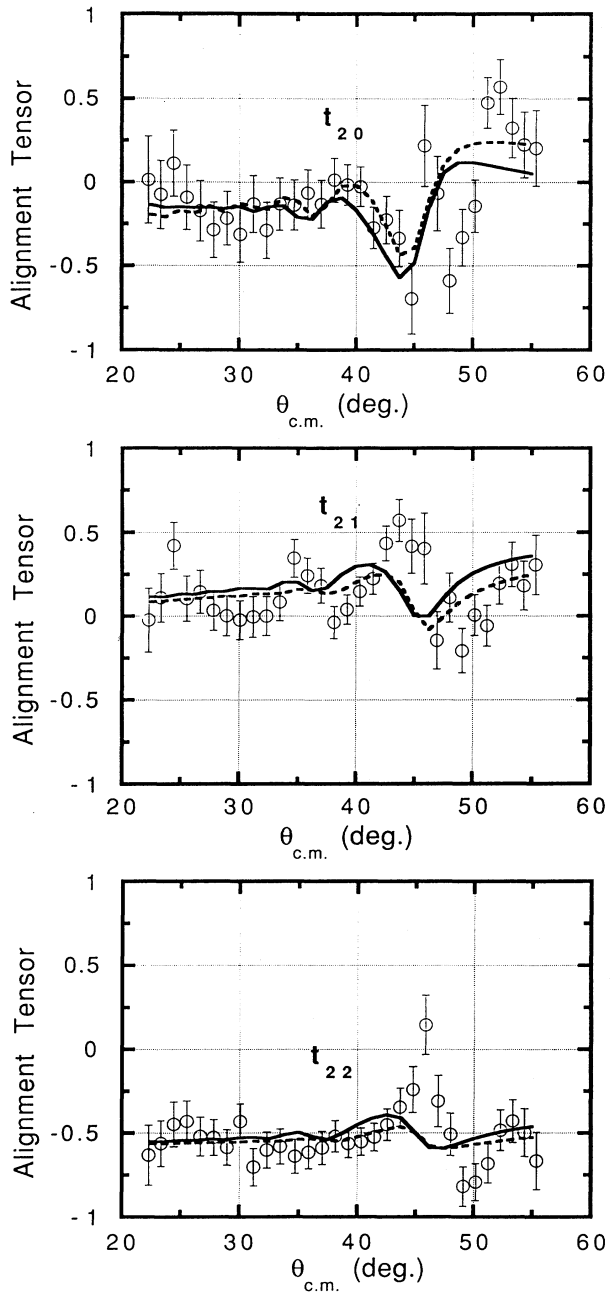


FIG. 8. Alignment tensors $t_{kq}$ for the $2_2^+ \rightarrow 2_1^+$ $\gamma$ decay of the $2_2^+$(2.94 MeV) state of $^{26}$Mg excited by 200 MeV $^{26}$Mg+$^{208}$Pb scattering as a function of c.m. scattering angle. The data, open circles, come from fitting Eq. (1) to the measured particle-$\gamma$ angular-correlation data assuming a mixing ratio of 0.12. The solid curve in each panel represents the best coupled-channels fit to all the differential cross-section and particle-$\gamma$ angular-correlation data using symmetric-rotor-model form factors for all the matrix elements shown in Fig. 1. Hyperfine attenuation of the original alignment was accounted for by normalizing the calculation to the data in the Coulomb-dominated region, $\theta_{c.m.} \leq 35°$. The dashed curve in each panel results from vibrational-model calculations where only an $M(l=0;2_1^+ \leftrightarrow 2_2^+)$ matrix element was used to connect the two $2^+$ states. The dashed curve also represents results from an asymmetric-rotor-model calculation.

ing proceeded by determining the values of the best defined parameters first and the fits shown are the end result.

Elastic scattering presented as ratio to Rutherford scattering is shown in Fig. 2. Coulomb scattering dominates out to about 40° and all cross sections are normalized to Rutherford at small angles. It is this absolute normalization to Rutherford scattering together with $4^+$ differential cross-section data and particle-$\gamma$ angular-correlation information that makes the present set of data unique. The principal uncertainty for the normalization comes from a 0.05° uncertainty in laboratory scattering angle and a 0.2-MeV uncertainty in the beam energy at the center of the target. A shallow real potential, about 25 MeV, and a deep real potential, about 200 MeV, were tried, together with their corresponding imaginary potentials. They give the same results for both the fit to all the differential cross sections and for the values of the matrix elements. In defining the optical potential, we relate the nuclear deformation parameters $\beta_l^n$ to the charge deformation parameters $\beta_l^c$ using the scaling procedure suggested by Hendrie.[6] We also examined the effect of using $\beta R$ scaling rather than Hendrie scaling to relate the nuclear matter shape to the nuclear charge shape. Although this scaling procedure leads to quite different nuclear deformation parameters for the highly deformed $^{26}$Mg nucleus, the calculated differential cross sections, alignment tensors, and matrix elements remain essentially unchanged. The shallow potential producing the fit shown as the solid curve in Fig. 2 is $V=21.45$ MeV, $W=22.28$ MeV, $r_0=1.277$ fm, $r'=1.300$ fm, $a=0.625$ fm, $a'=0.440$ fm.

### B. First $2^+$ state (1.81 MeV)

For the initial analysis of the $2_1^+$ state, we simplified the coupling scheme in Fig. 1 to include only the ground state and the first excited state. We made 1% steps in the value of $M(E2;0_1^+ \leftrightarrow 2_1^+)$ while searching, at each step, on $V$, $W$, $a$, $a'$, and the two reorientation matrix elements $M(E2;2_1^+ \leftrightarrow 2_1^+)$ and $M(E4;2_1^+ \leftrightarrow 2_1^+)$ to obtain a minimum-$\chi^2$ fit to the cross-section data of Figs. 2 and 3. At each of the steps, we compared the alignment tensors predicted by the coupled-channels fit to those measured (data points in Fig. 7), and computed a $\chi^2$ for fitting the alignment tensors. In comparing $(t_{kq})_{calc}$ with $(t_{kq})_{exp}$, we must correct $(t_{kq})_{calc}$ for the effect of hyperfine attenuation of the initial alignment.[7] We did this by comparing $(t_{kq})_{calc}$ with $(t_{kq})_{exp}$ in the Coulomb-dominated region, $\theta_{c.m.} \leq 35°$, for which we required $G_k(t_{kq})_{calc}=(t_{kq})_{exp}$, where $G_k$ is the hyperfine attenuation coefficient. This procedure gave $G_2=0.906\pm0.005$ and $G_4=0.687\pm0.005$. We assume these values hold over the entire angular range of the data and neglect a small systematic angular variation in the attenuation coefficients ($\Delta G_2/G_2<0.6\%, \Delta G_4/G_4<2\%$) due to a small change in charge state distribution (3% change in the $11^+$ charge state) of the emerging $^{26}$Mg ions over the angular range 25°–55°. Statistical experimental errors were adjusted by a scaling factor so that the $\chi^2$ for the

best fit to a particular data set was equal to the number of data points in that data set. In combining $\chi^2$ for the fit to the alignment tensors to the sum of $\chi^2$ for fitting the elastic and inelastic scattering to obtain a total $\chi^2$, we considered the eight alignment tensors at one angle to be a single measurement of the alignment at that angle on a par with the elastic and inelastic cross sections at that angle. Treating the errors in this manner, we show in Table I the values of the matrix elements that minimize total $\chi^2$ for three different calculations. In these calculations, the basic $M(E4)$ matrix element was held fixed at the value $+95$ $e$ fm$^4$, a determination that is explained in Sec. III E. The first row results from an analysis which uses only the Coulomb-dominated data, $\theta_{\text{c.m.}} \leq 35°$, the second

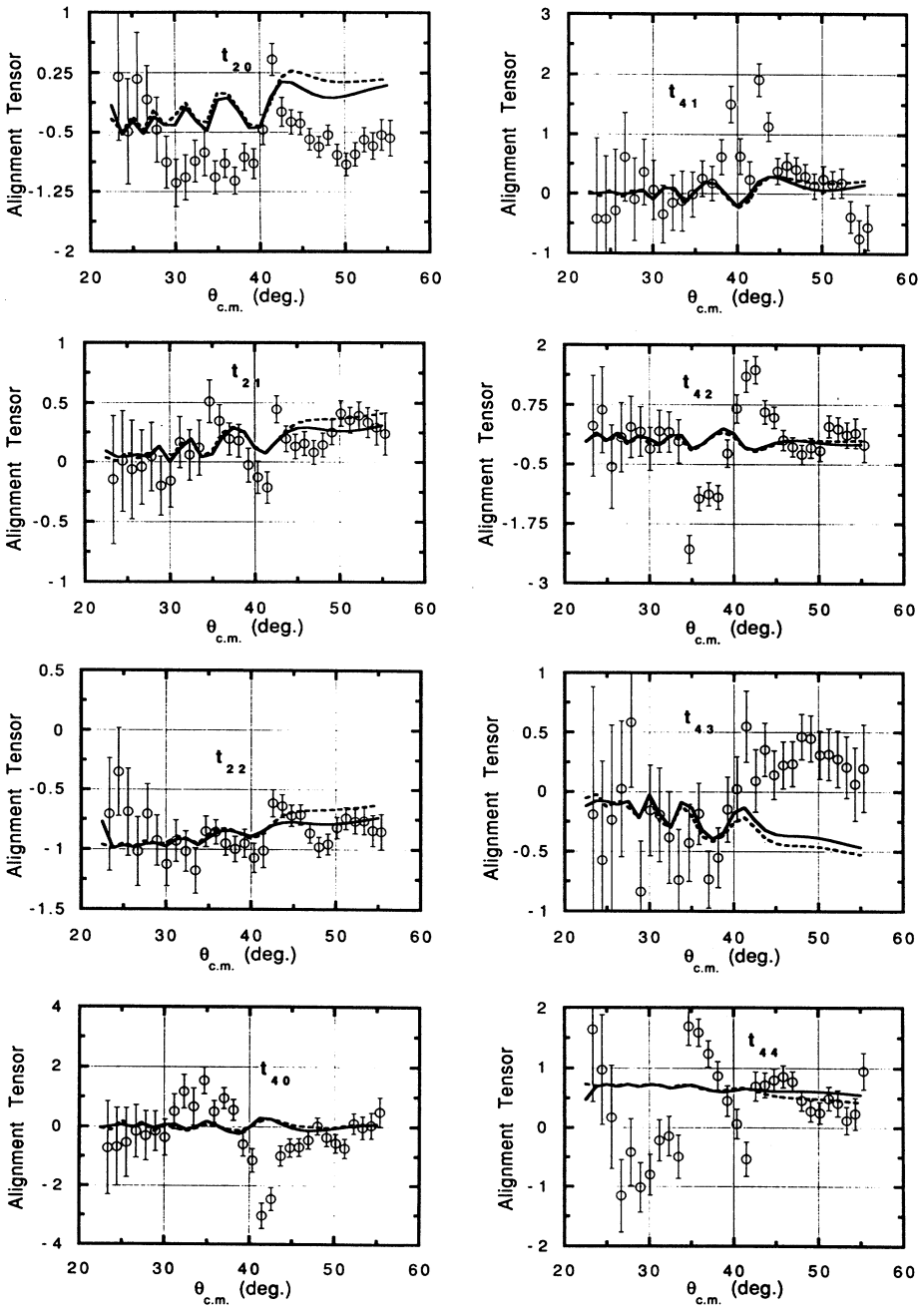


FIG. 9. Alignment tensors $t_{kq}$ for the $4_2^+ \rightarrow 2_1^+$ $\gamma$ decay of the $4_2^+$(4.90 MeV) state of $^{26}$Mg excited by 200 MeV $^{26}$Mg+$^{208}$Pb scattering as a function of c.m. scattering angle. The data, open circles, come from fitting Eq. (1) to the measured particle-$\gamma$ angular-correlation data. The solid curve in each panel represents the best coupled-channels fit to all the differential cross-section and particle-$\gamma$ angular-correlation data using symmetric-rotor-model form factors for all the matrix elements shown in Fig. 1. The dashed curve in each panel shows the effect on the calculated alignment for a 20% increase in the $M(E2;2_1^+ \leftrightarrow 4_2^+)$ matrix element.

TABLE I. Comparison of three coupled-channels analyses of the data. See text for details.

| Type of calculation | $M(E2;0_1^+\leftrightarrow 2_1^+)$ ($e$ fm$^2$) | $Q_2$ ($e$ fm$^2$) | $M(E4;2_1^+\leftrightarrow 2_1^+)$ ($e$ fm$^4$) |
|---|---|---|---|
| Coul. only; 2 states | $-16.86\pm0.13$ | $-23.5\pm3.8$ | $+323\pm133$ |
| All angles; 2 states | $-16.73\pm0.07$ | $-21.9\pm1.5$ | $+342\pm67$ |
| All angles; 5 states | $-16.79\pm0.18$ | $-20.9\pm1.9$ | $+304\pm95$ |

row comes from considering the entire angular range of the data, $\theta_{c.m.}\leq 55°$, and the third row shows the results for the same analysis, i.e., using the entire angular range, but including the $2_2^+$, $4_1^+$, and $4_2^+$ states as well. The errors indicated in the first two rows are statistical errors and include the effects of correlations with the other parameters. In addition to the contribution from correlations with the other parameters, the errors shown in the third row include contributions, added in quadrature, for the uncertainty in the absolute cross-section normalization, the uncertainty in the hyperfine attenuation coefficients, and the uncertainty in the alignment of the beam axis relative to the SS axis ($\pm0.5°$). The latter two uncertainties primarily affect the reorientation matrix elements. In Table I, the $E2$ reorientation matrix element is expressed as a static quadrupole moment, $Q_2$, using the relation

$$M(E2;2_1^+\leftrightarrow 2_1^+)=-[(5/16\pi)\tfrac{35}{2}]^{1/2}Q_2 \ . \tag{2}$$

Throughout this paper we use the sign convention adopted in the program ECIS.[5] The Coulomb values are consistent with the values from the analysis over the entire angular range. The smaller uncertainties in the second row relative to those in the first row reflect the increase in the number of data points used as well as an increased sensitivity due to structure in the data in the Coulomb-nuclear interference region, $\theta_{c.m.}\geq 35°$. Differences between third row and second row values in Table I reflect the effect of including the other states in the analysis. The solid curves in Figs, 2, 3, and 7 come from the analysis shown in the third row and the potential given above.

### C. Second $2^+$ state (2.94 MeV)

In Coulomb-excitation reorientation determinations of $Q_2$ there is an ambiguity in the magnitude depending on whether there is constructive or destructive interference from the $2_2^+$ state. In the case of $^{26}$Mg, it is claimed[8,9] that this ambiguity results in an uncertainty of 25–30% in the value of $Q_2$ determined from Coulomb excitation. This ambiguity does not appear in the present determination, third row in Table I, because the differential cross section for the $2_2^+$ state was measured and was specifically included in the analysis. The present data in the Coulomb-nuclear interference region are sensitive to the signs of the matrix elements involved and serve to resolve this ambiguity. Addition of the third $2^+$ state at 4.84 MeV had no noticeable effect on the extracted value $Q_2$; however, addition of a $2^+$ state at 15.8 MeV, which would be the location for the centroid of the giant quadrupole resonance (GQR) from simple systematics, with 60% of the sum-rule strength,[10] could increase $Q_2$ by 2–4% depending on the sign of the $2_1^+\leftrightarrow$GQR matrix element.

From the coupled-channels analysis using symmetric-rotor-model form factors, we obtain the fit shown as the solid curve in Fig. 4 and the following values for the pertinent matrix elements:

$$M(E2;0_1^+\leftrightarrow 2_2^+)=+2.89\pm0.09\ e\ \text{fm}^2 \ , \tag{3}$$

$$M(E2;2_1^+\leftrightarrow 2_2^+)=-11.4\pm1.9\ e\ \text{fm}^2 \ , \tag{4}$$

$$M(E4;2_1^+\leftrightarrow 2_2^+)=+49\pm50\ e\ \text{fm}^4 \ , \tag{5}$$

$$M(E2;2_2^+\leftrightarrow 2_2^+)=-15\pm20\ e\ \text{fm}^2 \ , \tag{6}$$

$$M(E4;2_2^+\leftrightarrow 2_2^+)=-570\pm475\ e\ \text{fm}^4 \ . \tag{7}$$

The alignment tensors for the $2_2^+\rightarrow 2_1^+$ $\gamma$ decay predicted with these matrix elements are indicated by the solid curves in Fig. 8. The alignment data shown in Fig. 8 were derived by applying Eq. (1) to the observed particle-$\gamma$ angular correlation with the assumption that the $2_1^+\rightarrow 2_2^+$ decay mixing ratio is 0.12.[11] The resulting $(t_{4q})_{exp}$ tensor components have a larger scatter than the $(t_{2q})_{exp}$ components. They are consistent with zero over the entire angular range, as expected for a predominantly $M1$ transition, and are therefore not shown. Nevertheless, these data appear to be the first extensive particle-$\gamma$ angular correlation data for a $2_2^+\rightarrow 2_1^+$ $\gamma$ decay, except for particle backscattering near 180° following a suggestion by Litherland and Ferguson to limit the $m$-substate population in the final state.[13] The alignment tensors from a symmetric-rotor-model calculation, the solid curves in Fig. 8, give a good account of the data except possibly in the large-angle region. By fitting to the Coulomb-dominated region, we determine the hyperfine attenuation coefficient for the decay of the $2_2^+$ state to be $G_2=0.72\pm0.05$. As the $2_2^+\rightarrow 2_1^+$ decay is predominantly $M1$, we also performed vibrational-model calculations where only an $M(l=0;2_1^+\leftrightarrow 2_2^+)$ matrix element, to simulate the $\Delta l=0$ aspect of an $M1$ decay, was used to connect the two $2^+$ states. The alignment tensors resulting from such an analysis are shown by the dashed curves in Fig. 8 and represent a 30% improvement in $\chi^2$ over the rotational-model calculation (solid curves). This vibrational-model calculation offers only a fair representation of the first $2^+$ alignment tensors with a $\chi^2$ value some 70% larger than the symmetric-rotor-model fit.

The second $2^+$ state has been attributed to a possible

triaxial shape for $^{26}$Mg.[14,15] Indeed the asymmetric-rotor-model[16] calculation, shown as a dashed curve in Fig. 4, gives a fair representation of the shape of the differential cross section. However, the sign of the $E2$ matrix element between the two $2^+$ states predicted by the asymmetric-rotor model is opposite to the sign deduced from the rotational-model fit and the predicted $4^+$ cross section is a factor of three larger than either of the two observed $4^+$ states. The alignment tensors for the $2_2^+$ state predicted by this asymmetric-rotor-model calculation are essentially the same as for the vibrational model shown as the dashed curves in Fig. 8. However, the fit to the alignment tensors for the first $2^+$ state by the asymmetric-rotor-model calculation is a factor of two worse in $\chi^2$ compared to the symmetric-rotor-model fit. We conclude that the present data and analysis do not offer much support for $^{26}$Mg to have a triaxial shape as represented by the asymmetric-rotor model.[16]

### D. $4^+$ state (4.32 MeV)

The differential cross section for exciting the first $4^+$ state, Fig. 5, eludes description by the rotational model especially in the grazing angle region near $\theta_{\text{c.m.}}=43°$. The solid curve in Fig. 5 represents the best fit obtainable with rotational-model form factors. We conclude that this state is not part of the ground-state rotational band. Nevertheless, from fitting the general magnitude of the observed cross section, we can extract a value for the $M(E4;0_1^+\leftrightarrow 4_1^+)$ matrix element defined by

$$M(E4;0_1^+\leftrightarrow 4^+)=\int \rho(r,\theta)r^4 Y_{40}(\theta)d\tau \ . \tag{8}$$

We obtain the following value for this matrix element:

$$M(E4;0_1^+\leftrightarrow 4_1^+)=+80\pm 20 \ e\ \text{fm}^4 \ . \tag{9}$$

Because of the failure to fit the shape of the differential cross section, we refrain from quoting values for the other matrix elements involving this state.

### E. $4^+$ state (4.90 MeV)

The second $4^+$ state, whose differential cross section is shown in Fig. 6, is well described by the rotational model (solid curve). From this fit, we obtain the following value for the hexadecapole matrix element [defined by Eq. (8)]:

$$M(E4;0_1^+\leftrightarrow 4_2^+)=+95\pm 10 \ e\ \text{fm}^4 \ . \tag{10}$$

The fit to the magnitude of the $4_2^+$ differential cross section plays the largest role in this determination. Other pertinent matrix elements obtained from fitting both the differential cross section (Fig. 5) and alignment data (Fig. 9) are

$$M(E2;2_1^+\leftrightarrow 4_2^+)=-23.8\pm 0.8 \ e\ \text{fm}^2 \ , \tag{11}$$

$$M(E4;2_1^+\leftrightarrow 4_2^+)=-50\pm 40 \ e\ \text{fm}^4 \ , \tag{12}$$

$$M(E2;4_2^+\leftrightarrow 4_2^+)=+59\pm 15 \ e\ \text{fm}^2 \ , \tag{13}$$

$$M(E4;4_2^+\leftrightarrow 4_2^+)=+455\pm 300 \ e\ \text{fm}^4 \ , \tag{14}$$

where the above $E4$ matrix elements include the influence of the higher-order $l=6$ and $l=8$ multipole orders which were in the analysis.

In spite of large error bars, the inclusion of alignment-tensor data for this state played a significant role in limiting possible values for the $M(E2;2_1^+\leftrightarrow 4_2^+)$ matrix element, primarily through its influence on the calculated alignment at large angles. This is illustrated by the dashed curves in Fig. 9 showing the calculated alignment tensors for a 20% increase in this matrix element relative to the best-fit value represented by the solid curves. It should be noted that this is the first time such alignment data have been determined for a large range of scattering angles. The general behavior of the alignment data appears to be well represented by the calculation. These results, especially the successful account of the differential cross section (Fig. 6), are convincing evidence that the 4.90 MeV state, not the 4.32 MeV state, is the $4^+$ member of the ground-state rotational band. This result confirms a similar conclusion of Clarke[17] and of Dybdal *et al.*[18] The hexadecapole matrix element, Eq. (10), then relates directly to the shape of the ground-state charge distribution. For a charge-radius parameter of 1.2 fm, the values of $M(E2;0_1^+\leftrightarrow 2_1^+)$ and $M(E4;0_1^+\leftrightarrow 4_2^+)$ determined here for the ground-state rotational band imply charge-deformation parameters of $\beta_2^c=+0.386$ and $\beta_4^c=+0.041$.

TABLE II. Comparison of various measurements and theoretical predictions for properties of the ground-state rotational band of $^{26}$Mg.

| Reaction or theory | $M(E2;0_1^+\leftrightarrow 2_1^+)$ ($e$ fm$^2$) | $Q_2$ ($e$ fm$^2$) | $M(E4;0_1^+\leftrightarrow 4_2^+)$ ($e$ fm$^4$) |
|---|---|---|---|
| $^{26}$Mg+$^{208}$Pb, 200 MeV (this work) | −16.79±0.18 | −20.9±1.9 | +95±10 |
| $^{37}$Cl+$^{26}$Mg (Ref. 8) | −17.2±0.4 | −12±4 or −16±4 | |
| $^{26}$Mg+$^{208}$Pb, 80–120 MeV (Ref. 9) | −17.9±0.4 | −9.5±3.0 or −13.6±3.0 | |
| $^{26}$Mg($e,e'$), 120 MeV (Ref. 19) | −16.58±0.13 | | +161±35 |
| Coulomb excitation[20] | −17.46±0.37 | | |
| Hartree-Fock[21] | −20.1 | −18.1 | |
| Shell model[22] | −19.9 | −14.7 | +134 |
| Asymmetric rotor[14] | −16.7 | −13 | |

## IV. DISCUSSION OF RESULTS

Table II summarizes the basic nuclear-structure information for the ground-state rotational band, $M(E2;0_1^+ \leftrightarrow 2_1^+)$, $M(E4;0_1^+ \leftrightarrow 4_2^+)$, and $Q_2$, the static quadrupole moment of the first $2^+$ state, and compares our values to other determinations and to theoretical estimates. The present determination of $Q_2$, which is primarily dependent on particle-$\gamma$ angular correlations, is insensitive to systematic errors in $M(E2;0_1^+ \leftrightarrow 2_1^+)$,[2] a problem which has plagued determinations that primarily rely on cross-section measurements. The present work determines the sign of the product of

$$M(E2;0_1^+ \leftrightarrow 2_1^+)M(E2;0_1^+ \leftrightarrow 2_2^+)M(E2;2_1^+ \leftrightarrow 2_2^+) > 0$$

which picks out the smaller of the two entries for $Q_2$ in the second and third rows and worsens the discrepancy with the present determination of $Q_2$. The present experiment also disagrees with electron-scattering results, fourth row of Table II, as regards the charge shape of $^{26}$Mg implied by the differing values for the hexadecapole matrix element, $M(E4;0_1^+ \leftrightarrow 4_2^+)$. We illustrate the difference graphically in Fig. 10 where the solid curve shows the charge surface of $^{26}$Mg deduced from the present values of $M(E2;0_1^+ \leftrightarrow 2_1^+)$ and $M(E4;0_1^+ \leftrightarrow 4_2^+)$ compared to the electron-scattering results shown as a dashed curve. The curves assume a uniform charge distribution and a charge-radius parameter of 1.20 fm.

In conclusion, we have presented an extensive, interdependent, data set including particle-$\gamma$ angular correlations and differential cross sections normalized by Coulomb scattering at forward angles. We have subjected this data set to a coupled-channels analysis and have extracted $E2$ and $E4$ matrix elements. We found that the portion of data in the Coulomb-nuclear interference region provided a sensitivity to the signs of the matrix elements as well as an additional sensitivity to magnitudes by virtue of structure in the angular distributions.

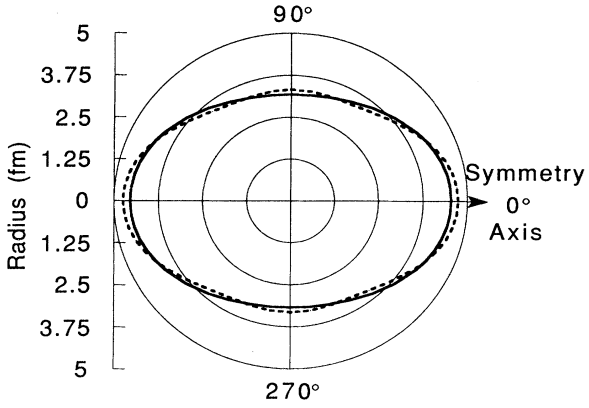


FIG. 10. The symmetric-rotor charge shape implied by electron scattering[18] (dashed curve) compared with the shape obtained from the present heavy-ion scattering data and analysis (solid curve) using a Coulomb-radius parameter of 1.2 fm.

## ACKNOWLEDGMENTS

We are grateful to J. B. McGrory for the shell-model results. The research at Western Kentucky University was supported by the National Science Foundation under Grant PHY-8519914. The research at Oak Ridge National Laboratory was supported by the U.S. Department of Energy under Contract No. DE-AC05-840R21400 with Martin Marietta Energy Systems, Inc.

[1]D. C. Hensley, E. E. Gross, M. L. Halbert, J. R. Beene, F. E. Bertrand, G. Vourvopoulos, D. L. Humphrey, and T. Van Cleve, Phys. Rev. C **40**, 2065 (1989).
[2]E. E. Gross, D. C. Hensley, and J. R. Beene, Phys. Rev. C **42**, R471 (1990).
[3]G. R. Satchler, *Direct Nuclear Reactions* (Clarendon, Oxford, 1983), p. 373.
[4]H. J. Rose and D. M. Brink, Rev. Mod. Phys. **39**, 306 (1967).
[5]J. Raynal, Phys. Rev. C **23**, 2571 (1981).
[6]D. L. Hendrie, Phys. Rev. Lett. **31**, 478 (1973).
[7]A. Abragam and R. V. Pound, Phys. Rev. **92**, 943 (1953).
[8]D. Schwalm, A. Bamberger, P. G. Bizzeti, B. Povh, G. A. P. Engelbertink, J. W. Olness, and E. K. Warburton, Nucl. Phys. **A192**, 449 (1972).
[9]R. H. Spear, T. H. Zabel, M. T. Esat, A. M. Baxter, and S. Hinds, Nucl. Phys. **A378**, 559 (1982).
[10]F. E. Bertrand, K. van der Borg, M. N. Harekeh, J. van der Plicht, and A. van der Woude, Phys. Rev. Lett. **40**, 635 (1978).
[11]P. M. Endt and C. van der Leun, Nucl. Phys. **A214**, 1 (1973).
[12]A. R. Poletti and E. K. Warburton, Phys. Rev. **137**, B595 (1965).
[13]A. E. Litherland and A. J. Ferguson, Can. J. Phys. **39**, 788 (1961).
[14]D. Kurath, Phys. Rev. C **5**, 768 (1972).
[15]R. De Leon, G. D'Erasmo, A. Pantaleo, M. N. Harakeh, S. Micheletti, and M. Pignanelli, Phys. Rev. C **23**, 1355 (1981).
[16]A. S. Davydov and G. F. Filippov, Nucl. Phys. **8**, 237 (1958).
[17]N. M. Clarke, J. Phys. G **6**, 865 (1980).
[18]K. Dybdal, J. S. Foster, P. Hornshøj, N. Rud, and C. A. Stroede, Nucl. Phys. **A359**, 431 (1981).
[19]E. W. Lees, A. Johnston, S. W. Brain, C. S. Curran, W. A. Gillespie, and R. P. Singhal, J. Phys. A **7**, 936 (1974).
[20]S. Raman, C. H. Malarkey, W. T. Milner, C. W. Nestor, and P. H. Stelson, Nucl. Data Tables **36**, 1 (1987).
[21]M. R. Gunye, Phys. Lett. **37B**, 125 (1971).
[22]J. B. McGrory, private communication.